Density Functional Embedded Cluster Calculations on Lewis Acid Centers of the α-Al$_2$O$_3$(0001) Surface: Adsorption of a CO Probe

VLADIMIR A. NASLUZOV,[1] VLADIMIR V. RIVANENKOV,[1] ALEXEY M. SHOR,[1] KONSTANTIN M. NEYMAN,[2] UWE BIRKENHEUER,[2,*] NOTKER RÖSCH[2]

[1]*Institute of Chemistry and Chemical Technology, Russian Academy of Sciences, 660049 Krasnoyarsk, Russia*
[2]*Institut für Physikalische und Theoretische Chemie, Technische Universität München, 85747 Garching, Germany*

ABSTRACT: We have investigated the adsorption of CO on the cation-terminated (0001) surface of α-Al$_2$O$_3$ with a generalized-gradient density functional approach. We used cluster models that are consistently embedded in an elastic polarizable environment (EPE), employing a (classical) shell model scheme and bare pseudopotentials (Al^{PP*}) for cations at the cluster boundary. The newly implemented EPE method was found to perform well for describing structure and adsorption properties of Lewis acidic centers of the polar (0001) surface known for its strong relaxation with respect to the bulk terminated geometry. The calculated data are stable with respect to the size of the cluster models. For the embedded stoichiometric clusters [Al$_4$O$_6$]/Al$_6^{PP*}$ and [Al$_{10}$O$_{15}$]/Al$_{13}^{PP*}$ of different structure, the adsorption induced shift $\Delta\nu$ of the CO stretching vibration and the binding energy (BE) are 30–42 cm^{-1} and 0.38–0.47 eV, respectively. The results for the frequency

shifts are in good agreement with the value of 39 cm^{-1} measured for CO/α-Al$_2$O$_3$(0001) at low coverages. Judged by the frequency shift and the adsorption energy, the interaction of CO molecules with three-coordinated Al^{3+} cations at the regular surface is very similar to that with Mg^{2+} corner sites of MgO polycrystallites, $\Delta \nu = 39$ cm^{-1}, BE = 0.38 eV.   © 2002 Wiley Periodicals, Inc. Int J Quantum Chem 90: 386–402, 2002

Introduction

Aluminium oxides (aluminas) of the general stoichiometric formula Al$_2$O$_3$ are successfully employed for various modern technologies [1, 2]. Aluminas with large effective surface area are widely used as a support for heterogeneous catalysts [3]. Metastable (transition) aluminas, like γ-Al$_2$O$_3$, exhibit themselves catalytic activity due to Lewis acidic sites (LAS). The latter sites can be efficiently probed by adsorption of CO molecules [4, 5]. Three types of LAS have been identified on γ-Al$_2$O$_3$ by blue shifts of the CO vibrational frequency $\Delta \nu$(CO) $\gtrsim$ 40 cm^{-1}. However, neither the structure nor the nature of these sites is well understood. These centers are formally assigned to Al^{3+} cations located at surface positions derived from the structural arrangement of the tetrahedral cavities between O^{2-} anions of the bulk [6, 7].

Based on calculations of molecular cluster models [8], these three types of centers have been assigned to three-, four-, and fivefold coordinated Al^{3+} cations. However, molecular cluster models are rather indirectly related to the specific structure of the surface under consideration. For instance, they do not distinguish between the surface centers of the same coordination on different aluminas. To overcome this limitation, embedded cluster models of LAS have to be designed to take the long-range order of the oxides into account. For alumina this is a particularly complicated task since only α- and κ-modifications of Al$_2$O$_3$ exhibit an ordered structure whereas other known modifications feature a random distribution of the cations over the partially occupied crystal positions. Large unit cells are required to describe such disordered systems in a consistent fashion, rendering first principles periodic slab model calculations very demanding.

A consistent cluster embedding approach for ionic substrates [9] should take the surface structure into account, e.g., as provided by force-field based molecular mechanical (MM), i.e., atomistic simulations (AS) [10–12]. Since accurate experimental structural information on the surface sites of transition aluminas is lacking, it is preferable to validate a novel embedding method as the one described here first for a related well characterized surface. The most thoroughly studied alumina surface, α-Al$_2$O$_3$(0001), has a rather simple structure and often serves as a touchstone for analyzing the performance of computational techniques. Several band structure (periodic boundary) calculations of this system have been reported recently [13–18]. Here, we have chosen α-Al$_2$O$_3$(0001) and related adsorption complexes with a CO probe molecule to validate the recently developed elastic polarizable environment (EPE) method for a consistent cluster embedding of ionic crystals [9].

α-Al$_2$O$_3$ (corundum, sapphire) is thermodynamically stable and exhibits a regular and highly stoichiometric crystalline structure featuring hexagonal close-packing of oxygen anions [19, 20]. This alumina modification is well described as a highly ionic large band gap insulator with the charge of cations and anions close to +3e and −2e, respectively [21]. This characterization is supported by atomistic simulations [22–25] as well as by quantum mechanical density functional (DF) and Hartree–Fock (HF) calculations [14, 26–30]. Many features of the electronic structure of ionic metal oxides with the rock salt structure (in particular, those relevant to the description of their surface properties) can be reproduced to a good approximation using cluster models under the influence of the external electrostatic field caused by the crystal environment [31]. However, more effort is required to design suitable surface models of α-alumina which does not exhibit dense stoichiometric crystallographic planes. Rather, the bulk-terminated structure is unstable and undergoes significant reconstruction [32]—hence, bulk-terminated surface models of α-alumina are inadequate. This statement holds in general for metal oxide surfaces formed along polar (nonstoichiometric) crystallographic planes.

Detailed experimental information on the structure of polar surfaces of oxides is scarce [33]; α-Al_2O_3(0001) is one of few exceptions [34]. α-Al_2O_3(0001) is a so-called charge-neutralized polar surface where the relaxation of the bulk-terminated structure is particularly significant [32]. The importance of relaxation has also been shown by recent experiments on transition metal congeners of α-Al_2O_3, α-Cr_2O_3 [35], and α-Fe_2O_3 [16].

One of the principal questions is whether a polar surface is terminated by cations or by anions [36]. When a crystal is cleaved to form a polar surface, the type of termination defines the value and direction of the surface dipole moment and the extent of the subsequent relaxation. The remaining dipole moment affects the adsorption properties of the surface [37]. From a refinement of the grazing incidence X-ray scattering (GIXS) data, it has been concluded that the α-Al_2O_3(0001) surface is terminated by a single layer of Al^{3+} cations [34]. This finding has also been supported by a combined study based on the time-of-flight scattering, recoiling spectrometry, and classical ion trajectory simulations [38] as well as by low-energy electron diffraction [39]. From molecular mechanic [24] and molecular dynamics [10] simulations the cation-terminated (0001) surface of α-alumina is known to be the most stable one. The preferred stability of this surface as compared to surfaces terminated by oxygen anions was also corroborated in a DF study [17]. Termination by metal cations is also favored for the (0001) surface of the iso-structural α-Cr_2O_3 [35].

Besides serving as a benchmark for developing theoretical models, the (0001) surface of α-Al_2O_3 exposing threefold coordinated Al^{3+} centers can profitably be employed as an example system for studying Lewis acid centers at the surfaces of other structurally related ionic oxides. We mention the (111) surface of γ-Al_2O_3, where the packing of O^{2-} ions results in a threefold coordination of the cations. A regular model of the cation-terminated (111) surface exhibits a 1:4 ratio of Al^{3+} to O^{2-} ions, at variance with the 1:3 ratio of the (0001) surface of α-Al_2O_3. Relaxation of the bulk-terminated α-Al_2O_3(0001) surface reduces the dipole moment, mainly due to a shortening of the first Al–O interplane distance. For γ-Al_2O_3(111), one expects other mechanisms, like the redistribution of cations over fractionally occupied positions, to contribute to the quenching of the surface dipole moment [5, 40]. One should keep in mind that hydroxylation also affects the surface properties in many practical situations, but here we restrict ourselves to clean oxide surfaces only. Also, α-Al_2O_3(0001) is structurally related to the well-ordered aluminium oxide films that are formed by oxidation of NiAl(110) and used to study supported metal particles on oxides [41]. Similarly, alumina films grown on W(110) are proposed to be either Al-terminated α-Al_2O_3(0001) or γ-Al_2O_3(111) [42]. Thus, a clarification of the properties of the (0001) surface of α-alumina will assist in improving our understanding of the characteristics of other important oxide surfaces.

Few cluster calculations of surface species on oxides with proper embedding have been attempted up to now. Recently, we have presented the EPE method for a consistent cluster embedding of ionic crystals [9]; this new approach has been implemented in the parallel density functional program PARAGAUSS [43, 44]. The EPE method considers a quantum mechanical (QM) cluster as a defect in a shell-model (MM or AS) treatment [45, 46] of the surrounding oxide. It allows a (formally) unrestricted geometry optimization of the cluster as well as of the lattice environment which responds to the perturbations due to changes in the cluster relative to a reference model of the regular crystal. The EPE approach was employed to study the structure and the properties of the O^{2-} site as well as neutral and charged oxygen vacancies on the MgO(001) surface; also, the adsorption of a palladium atom on these sites has been investigated [9].

Below we will outline the combined QM/MM(AS) approach for investigating adsorption properties of the polar surface α-Al_2O_3(0001) and we will apply the method to study CO adsorption as a probe molecule of LAS. We will address the following issues:

- Does the EPE embedding procedure provide reasonably fast convergence of the results with increasing size of the QM clusters?
- Does the AS approach employed yield a sufficiently accurate description of the charge distribution and the relaxation of the surface α-Al_2O_3(0001) to provide adequate boundary conditions for cluster models of adsorption sites on the oxide?
- Are low-coordinated cations on the (0001) surface responsible for the known Lewis acidity of α-Al_2O_3?

To the best of our knowledge, we report here the first QM calculations of the adsorption system CO/Al_2O_3 that employs an approach based on model clusters which are embedded in an environ-

ment that represents both the mechanical and electric properties of the α-Al$_2$O$_3$(0001) surface. Other computational investigations of LAS on α-alumina utilized point charge embedded cluster models [47, 48] or periodic slab models [18, 49, 50]. According to the latter studies, the LAS on the clean surface α-Al$_2$O$_3$(0001) are strong enough to favor dissociative adsorption of H$_2$O over molecular adsorption.

We shall first present an overview of the computational strategy and details of the EPE calculations. Then we will describe the results of the calculations, comparing pure MM(AS) and embedded cluster structures of α-Al$_2$O$_3$. Finally, the results on LAS adsorption complexes with CO will be discussed.

EPE Embedding

The pertinent features of the EPE cluster embedding can be described as follows [9]. (i) The structure of a regular (unperturbed) surface is defined by classical atomistic simulations of a periodic slab model of the surface; (ii) an unperturbed surface site is described by a QM cluster, embedded in such a slab represented as an elastic polarizable environment; (iii) the surface site under investigation (e.g., an adsorption complex, defect center) is treated as a defect of the regular periodic structure [45, 46]; (iv) both the long-range Coulomb coupling and the short-range interactions of the QM and classical regions are explicitly taken into account and the structure of the whole system is determined variationally by minimizing the total energy.

The effect of environment on the QM cluster is given by the Madelung field of this environment and by the short-range forces of the AS model at the cluster boundary. The QM/MM(AS) interface is constructed in such a way that the environment responds to changes of the defect cluster relative to the situation at the regular surface (regular site). Special measures are taken so that the environment retains its AS equilibrium structure if a cluster representing the regular site is embedded. In general, both the cluster and its environment undergo a relaxation due to changes caused, for instance, by an adsorbate. The EPE embedding avoids pitfalls of the cluster approach that can arise from somewhat arbitrary constraints of the adsorption induced relaxation.

According to the EPE embedding procedure [9], the system under consideration—here a slab of α-Al$_2$O$_3$(0001)—is partitioned into the active area, Region I, and its environment, Region II (Fig. 1).
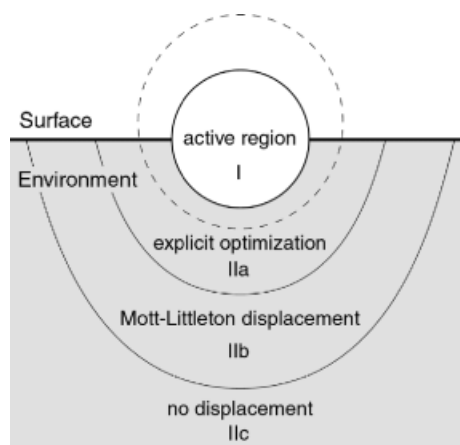

FIGURE 1. Sketch of the space partitioning underlying the EPE embedded cluster model treatment of a surface site. Region I—internal region of QM treatment in Steps 2 and 3 of the embedding procedure. Region II represents the shell-model environment of the QM cluster in Steps 2 and 3 of the embedding procedure. Subregions: IIa—region of explicit optimization, IIb—region described by the effective polarization given by Mott–Littleton displacements, IIc—external environment, energy contribution due to the interaction of a (potential) charge monopole centered at the defect with induced dipole moments on ions of the environment, but without any displacements of the ions. Subregions IIb and IIc are distinguished in the case of a charged defect only. The sphere of the auxiliary surface charge distribution to represent the Madelung field acting on the QM cluster is shown by a dashed line.

Region II is described classically: the mechanic and electric relaxation of the environment is taken into account by a shell-model description combined with the Mott–Littleton approach [45, 46]. Region I comprises the QM cluster model including, if present, an adsorbate and pseudopotential centers which describe atoms of the boundary region. In the EPE method, the total energy, E_{tot}, of the system is a sum of the three contributions:

$$E_{\text{tot}} = E_{\text{cl}} + E_{\text{int}} + E_{\text{lat}}, \tag{1}$$

where E_{cl}, E_{int}, and E_{lat} describe the intracluster interactions, the coupling of the QM cluster and the environment, and the intralattice interactions, respectively. The following preparatory computational Steps 1 and 2 need to be performed once, before QM/EPE calculations are carried out as Step 3 [9].

In Step 1 a purely MM(AS) treatment of the *regular* (*unperturbed*) surface is performed. The structure of the surface is calculated by minimizing the total

energy $E_{\text{tot}}^{\text{MM}}$ of a repeated slab using the shell-model scheme [46]. $E_{\text{tot}}^{\text{MM}}$ depends on the coordinates R and on the effective dipole moments μ of the shell-model ions, each of the latter represented by two point charges of opposite signs (a core and a shell) that are connected by a "spring" with a force constant adjusted to describe the polarizability of the ion in electrostatic field,

$$E_{\text{tot}}^{\text{MM}}(R, \mu) \stackrel{\text{minimization}}{\Longrightarrow} R^{\text{reg}}, \mu^{\text{reg}}. \qquad (2)$$

The superscript reg labels the AS geometry (and the electrostatic potential) of the *regular* surface, unperturbed by any defect or adsorbate.

One has to differentiate three types of ions: those located at the regular centers of the QM cluster, R_{cl}, ions at pseudopotential centers, R_{pp}, and ions at lattice positions of the environment (Region II), R_{lat}. In Steps 2 and 3, the shell-model ions at R_{cl} and R_{pp} of Region I (Fig. 1) are substituted by real QM and pseudopotential ions, respectively. Without implying any further calculations, Eq. (2) is reformulated for these three types of ions as

$$
\begin{aligned}
E_{\text{tot}}^{\text{MM}}&(R_{\text{cl}}, R_{\text{pp}}, R_{\text{lat}}, \mu_{\text{cl}}, \mu_{\text{pp}}, \mu_{\text{lat}}) \\
&\stackrel{\text{minimization}}{\Longrightarrow} \begin{array}{l} R_{\text{cl}}^{\text{reg}}, R_{\text{pp}}^{\text{reg}}, R_{\text{lat}}^{\text{reg}}, \\ \mu_{\text{cl}}^{\text{reg}}, \mu_{\text{pp}}^{\text{reg}}, \mu_{\text{lat}}^{\text{reg}}, \\ \rho_{\text{cl}}^{\text{tot,MM}}(R_{\text{cl}}^{\text{reg}}, R_{\text{pp}}^{\text{reg}}, \mu_{\text{cl}}^{\text{reg}}, \mu_{\text{pp}}^{\text{reg}}). \end{array}
\end{aligned} \qquad (3)
$$

The optimized coordinates and dipole moments of the shell-model ions in Region I as well as the electrostatic potential of the resulting charge distribution, $\rho_{\text{cl}}^{\text{tot,MM}}(R_{\text{cl}}^{\text{reg}}, R_{\text{pp}}^{\text{reg}}, \mu_{\text{cl}}^{\text{reg}}, \mu_{\text{pp}}^{\text{reg}})$, represent the reference to be used in Step 3. The configuration of the shell-model ions in Regions II will be used in Step 2.

Step 2 provides the QM *reference* of the unperturbed cluster (Region I; without an adsorbate etc.) *embedded* in the *regular* environment of the frozen lattice configuration. The expression for the variable part of the energy E_{tot} (without the fixed contribution E_{lat}) reads

$$
\begin{aligned}
E_{\text{clean surface}}^{\text{QM,reg emb}}(\rho_{\text{cl}}, R_{\text{cl}}, R_{\text{pp}}) &= E_{\text{cl}} + E_{\text{int}}^{\text{bare}} \\
E_{\text{cl}} &= E^{\text{QM}}(\rho_{\text{cl}}, R_{\text{cl}}) + \text{tr}(\rho_{\text{cl}} V_{\text{pp}}(R_{\text{pp}})) \\
&\quad + V_{\text{nn}}^{\text{mod}}(R_{\text{cl}}, R_{\text{pp}}) \\
E_{\text{int}}^{\text{bare}} &= [\rho_{\text{cl}}^{\text{tot,QM}}(\rho_{\text{cl}}, R_{\text{cl}}, R_{\text{pp}}) \| \rho_{\text{lat}}(R_{\text{lat}}^{\text{reg}}, \mu_{\text{lat}}^{\text{reg}})] \\
&\quad + V_{\text{short}}(R_{\text{cl}}, R_{\text{pp}}, R_{\text{lat}}^{\text{reg}}).
\end{aligned} \qquad (4)
$$

Here $\rho_{\text{cl}}^{\text{tot}}$ and ρ_{cl} are the total charge density (i.e., the electron density plus the atomic nuclei) and the electron-only contribution of Region I, respectively; ρ_{lat} is the total charge density of Region II,

comprising the core and shell charges of all those shell-model ions. $\text{tr}(\rho V)$ denotes the energy of an electronic charge distribution ρ in a potential V; $[\rho_1 \| \rho_2]$ designates the Coulomb interaction energy between the charge distributions ρ_1 and ρ_2. Besides the genuine QM cluster contribution E^{QM}, the cluster energy E_{cl} comprises the interaction of the cluster electronic charge density ρ_{cl} with the field V_{pp} of the pseudopotential centers and a modified nuclear repulsion term $V_{\text{nn}}^{\text{mod}}$ between the atoms of the cluster and the pseudopotential centers at R_{pp} (see below). This modification is necessary to counter possible deficiencies of the pseudopotential description when reproducing the geometry of the QM cluster. The energy $E_{\text{int}}^{\text{bare}}$ contains the Coulomb interaction between the (total) charge distributions of both regions as well as a short-range term V_{short} adapted from pure shell-model treatment. That latter potential energy V_{short} originates from the genuine short-range interaction contributions to the interregion coupling energy E_{int} of the shell model.

Optimizing the energy $E_{\text{clean surface}}^{\text{QM,reg emb}}(\rho_{\text{cl}}, R_{\text{cl}}, R_{\text{pp}})$, Eq. (4), with respect to the electronic charge density ρ_{cl} and the positions of the cluster ions R_{cl} and R_{pp} (by a QM calculation) provides the *reference* configuration (hence the notation ref) of the QM cluster model embedded in the unperturbed clean surface, $R_{\text{lat}} = R_{\text{lat}}^{\text{reg}}$, $\mu_{\text{lat}} = \mu_{\text{lat}}^{\text{reg}}$ (Region II):

$$
\begin{aligned}
E_{\text{clean surface}}^{\text{QM,reg emb}}&(\rho_{\text{cl}}, R_{\text{cl}}, R_{\text{pp}}) \\
&\stackrel{\text{minimization}}{\Longrightarrow} \rho_{\text{cl}}^{\text{ref}}, R_{\text{cl}}^{\text{ref}}, R_{\text{pp}}^{\text{ref}}, \rho_{\text{cl}}^{\text{tot,QM}}(\rho_{\text{cl}}^{\text{ref}}, R_{\text{cl}}^{\text{ref}}, R_{\text{pp}}^{\text{ref}}).
\end{aligned} \qquad (5)
$$

The total charge distribution of the reference configuration $\rho_{\text{cl}}^{\text{tot,QM}}(\rho_{\text{cl}}^{\text{ref}}, R_{\text{cl}}^{\text{ref}}, R_{\text{pp}}^{\text{ref}})$ obtained here is different from $\rho_{\text{cl}}^{\text{tot,MM}}(R_{\text{cl}}^{\text{reg}}, R_{\text{pp}}^{\text{reg}}, \mu_{\text{cl}}^{\text{reg}}, \mu_{\text{pp}}^{\text{reg}})$ associated with Region I by the pure MM treatment of the clean surface in Step 1—and so are the electrostatic potentials experienced by the surrounding environment.

In Step 3 one performs QM/EPE calculations of an active region modified by the presence of an adsorbate, a defect, or both. If one would minimize the total energy

$$
\begin{aligned}
E_{\text{tot}}^{\text{bare}} &= E_{\text{cl}} + E_{\text{int}}^{\text{bare}} + E_{\text{lat}} \\
E_{\text{lat}} &= E_{\text{intra-lat}}^{\text{MM}}(R_{\text{lat}}, \mu_{\text{lat}}),
\end{aligned} \qquad (6)
$$

even *without any defect*, a *relaxation* of Region II would result because of the difference between $\rho_{\text{cl}}^{\text{tot,MM}}(R_{\text{cl}}^{\text{reg}}, R_{\text{pp}}^{\text{reg}}, \mu_{\text{cl}}^{\text{reg}}, \mu_{\text{pp}}^{\text{reg}})$, Eq. (3), and $\rho_{\text{cl}}^{\text{tot,QM}}(\rho_{\text{cl}}^{\text{ref}}, R_{\text{cl}}^{\text{ref}}, R_{\text{pp}}^{\text{ref}})$, Eq. (5). To avoid this artifact, $E_{\text{int}}^{\text{bare}}$ is modified by defining an effective (total) charge density $\rho_{\text{cl}}^{\text{tot,eff}}(\rho_{\text{cl}}, R_{\text{cl}}, R_{\text{pp}})$ to be used in place of $\rho_{\text{cl}}^{\text{tot,QM}}$ in Eq. (6) such that, for a refer-

ence configuration of a defect-free system, $\rho_{cl}^{tot,eff}$ coincides with $\rho_{cl}^{tot,MM}(R_{cl}^{reg}, R_{pp}^{reg}, \mu_{cl}^{reg}, \mu_{pp}^{reg})$ of the substrate in its *regular* structure:

$$
\begin{aligned}
\rho_{cl}^{tot,eff}&(\rho_{cl}, R_{cl}, R_{pp}) \\
&= \rho_{cl}^{tot,QM}(\rho_{cl}, R_{cl}, R_{pp}) - \rho_{cl}^{tot,QM}(\rho_{cl}^{ref}, R_{cl}^{ref}, R_{pp}^{ref}) \\
&\quad + \rho_{cl}^{tot,MM}(R_{cl}^{reg}, R_{pp}^{reg}, \mu_{cl}^{reg}, \mu_{pp}^{reg}). \quad (7)
\end{aligned}
$$

Analytic representations of $\rho_{cl}^{tot,MM}(R_{cl}^{reg}, R_{pp}^{reg}, \mu_{cl}^{reg}, \mu_{pp}^{reg})$ and $\rho_{cl}^{tot,QM}(\rho_{cl}^{ref}, R_{cl}^{ref}, R_{pp}^{ref})$ generated in Steps 1 and 2, respectively, are used to construct $\rho_{cl}^{tot,eff}$ in the final QM/EPE calculations. An effective short-range potential is defined similarly:

$$
\begin{aligned}
V_{short}^{eff}&(R_{cl}, R_{pp}, R_{lat}) = V_{short}(R_{cl}, R_{pp}, R_{lat}) \\
&- V_{short}(R_{cl}^{ref}, R_{pp}^{ref}, R_{lat}) + V_{short}(R_{cl}^{reg}, R_{pp}^{reg}, R_{lat}). \quad (8)
\end{aligned}
$$

Again, in the absence of any surface defects, $V_{short}^{eff}(R_{cl}, R_{pp}, R_{lat})$ coincides with $V_{short}(R_{cl}^{reg}, R_{pp}^{reg}, R_{lat})$. The modified coupling energy E_{int}^{eff} is defined in analogy to E_{int}^{bare},

$$
\begin{aligned}
E_{int}^{eff} = \big[\rho_{cl}^{tot,eff}&(\rho_{cl}, R_{cl}, R_{pp}) \| \rho_{lat}(R_{lat}, \mu_{lat}) \big] \\
&+ V_{short}^{eff}(R_{cl}, R_{pp}, R_{lat}), \quad (9)
\end{aligned}
$$

where the first term represents the Coulomb interaction of Regions I and II. This modification does not directly affect the QM treatment because the electronic charge density ρ_{cl} enters the effective charge density $\rho_{cl}^{tot,eff}$ only via the bare QM cluster charge density $\rho_{cl}^{tot,QM}$. Finally, the EPE total energy of the whole system to be minimized reads (see Eq. (6))

$$
\begin{aligned}
E_{tot}^{EPE} &= E_{cl} + E_{int}^{eff} + E_{lat} \\
E_{tot}^{EPE}&(\rho_{cl}, R_{cl}, R_{pp}, R_{lat}, \mu_{lat}) \\
&\xRightarrow[\text{minimization}]{} \begin{array}{l} R_{cl}^{EPE}, R_{pp}^{EPE}, R_{lat}^{EPE}, \\ \rho_{cl}^{EPE}, \mu_{lat}^{EPE}. \end{array} \quad (10)
\end{aligned}
$$

The terms of this energy expression can be regrouped to yield

$$
\begin{aligned}
E_{tot}^{EPE} &= E_{cl} + E_{int}^{bare} + E_{lat}^{eff} \\
E_{lat}^{eff} &= E_{lat} + E_{int}^{corr}. \quad (11)
\end{aligned}
$$

The additional terms E_{int}^{corr} in the interaction energy due to the effective forms of the charge density and the short-range potential do not depend on coordinates of either the nuclei or the electrons of the QM cluster and thus these terms can formally be reassigned to the intralattice energy.

Computational Details

It is known that bulky diffuse O^{2-} anions as frontier centers of a QM cluster undergo a strong artificial polarization by neighboring positive point charges, thus inducing an erroneous electrostatic field at the modelled adsorption site [51–53]. Clusters with oxygen centers surrounded in the first co-ordination sphere by regular cations only are more reliable, but these clusters with an excess of cations are not stoichiometric. This can result in an undesirable withdrawal of electron density from the central part of the QM cluster. To avoid such artifacts, the cations of the boundary region are represented by bare pseudopotential centers Al^{3+} without any basis functions [51, 54]. In the following, such bare centers (described in this work by soft-core pseudopotentials [55]) will be labelled as Al^{PP*}. Here, the following EPE embedded cluster models of LAS at the α-$Al_2O_3(0001)$ surface will be studied under the symmetry constraints of the point group C_3 (Fig. 2): (a) $[Al_7O_3]^{15+}$ with anions coordinated by regular cations only; (b)–(d) minimal stoichiometric clusters $[Al_4O_6]/Al_6^{PP*}$, where the cations represented by bare Al^{PP*} centers are located at three different sites of the boundary region; (e), (f) extended stoichiometric clusters $[Al_{10}O_{15}]/Al_{13}^{PP*}$ with two variants of the Al^{PP*} positions. Since bare pseudopotentials interact with the electronic states of the cluster, they provide a repulsion which differs somewhat from that of the regular cations. To compensate for the distortion of the cluster geometry due to this difference, Buckingham-type pair potentials are added to correct the interaction of the anions with bare pseudopotential cations; this corrected interaction is given by $V_{nn}^{mod}(R_{cl}, R_{pp})$ in Eq. (4). The pair potentials parameterized to reproduce potential curves for the displacements of ions in the central part of the cluster $[Al_4O_6]Al_9^{PP*}$ are displayed in Table I; this cluster models a bulk site of α-Al_2O_3 (Fig. 3).

To generate the crystal environment of these clusters, a slab model of the *regular* α-$Al_2O_3(0001)$ surface has been optimized in Step 1 of the EPE procedure at the classical level in the rigid-ion mode (i.e., neglecting any polarization of the ions) using empirical parameters [56]. The unit cell parameters parallel to the surface were kept fixed at the bulk values; the height of the unit cell normal to the surface was set to 400 Å. Thus, only positions of ions within the fixed unit cell were optimized. This strategy accounts for constraints imposed by the bulk substrate on the surface layers of a crystal.
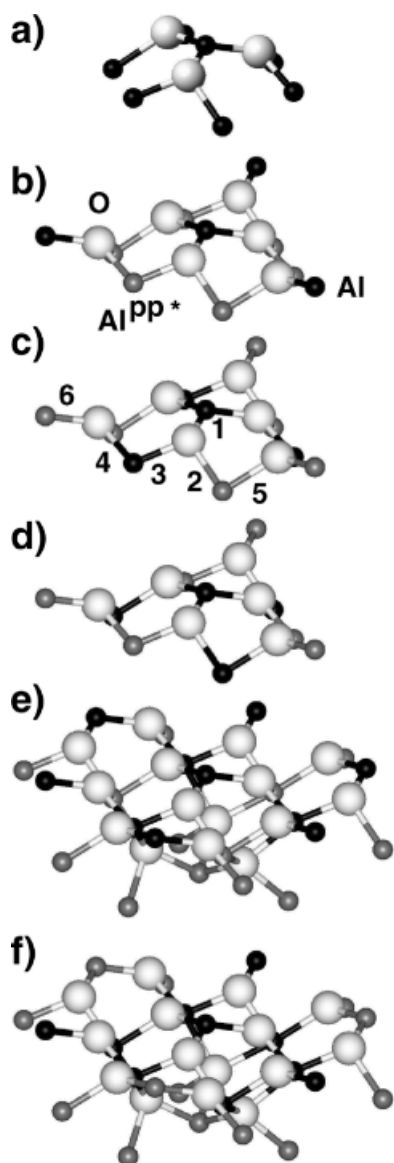
FIGURE 2. Cluster models (a) $[Al_7O_3]^{15+}$, (b)–(d) $[Al_4O_6]/Al_6^{pp*}$, and (e), (f) $[Al_{10}O_{15}]/Al_{13}^{pp*}$ for modeling LAS of α-Al_2O_3(0001). The bond lengths 1–6 labeled in panel (c) are displayed in Table VI.

TABLE I

Buckingham-type pair potential function $f(r) = A\exp(-Br) + Cr^{-6}$ for correcting the interaction $V_{nn}^{mod}(R_{cl}, R_{pp})$ of the bare pseudopotentials Al^{pp*} with oxygen centers of the QM cluster (see Fig. 3).

Interaction	Al^{pp*}-O
Reference anion cavity	Al1(1)Al2(2)O1(5)Al3(3)Al(−1)(4)
Target anion cavity	Al1(1)Al2(2)O1(5)Al3^{pp*}(3)Al(−1)^{pp*}(4)
Center displaced	O1(5)
Displacement direction[a]	$\vec{r}_5 \pm \frac{1}{2}(\vec{r}_1 + \vec{r}_2)$
A (a.u.)	11.78
B (a.u.)	0.5524
C (a.u.)	0.5964

[a] The vectors $\vec{r}_1$, $\vec{r}_2$, and $\vec{r}_5$ designate positions of the atoms Al1(1), Al2(2), and O1(5), respectively.

in the present work interact very weakly, indicating that the slab is sufficiently thick for studying adsorption properties. Indeed, according to test calculations, the vibrational frequency v(CO) of a CO probe molecule adsorbed at clusters embedded in 9L and 18L slabs differs by 2 cm^{-1} only. 9L slab models were utilized in previous first-principles supercell calculations of α-Al_2O_3(0001) [14, 42, 58] and
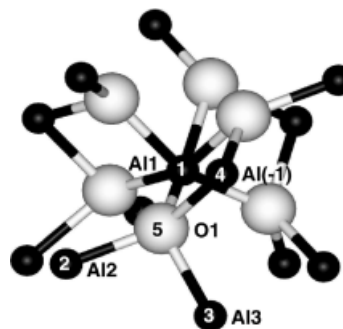
FIGURE 3. Cluster $[Al_4O_6]Al_8^{pp*}$ modelling bulk α-Al_2O_3 used for the paramentization of the correction pair potential V_{nn}^{mod}. Reference case: all cations are taken as regular atoms with basis functions; target case: cations 1 and 2 are regular atoms, cations 3 and 4 are pseudopotential centers Al^{pp*} without basis functions. Atomic labels given as numbers indicate the layer numbers in the slab model of the α-Al_2O_3(0001) surface displayed in Figure 4. Al(-1) is a cation of the (upper) layer, the neighbor of the layer Al1, that is removed upon crystal cleavage when the surface is created; therefore, Al(-1) is not shown Figure 4.

A minimum stoichiometric slab (MSS) model of α-Al_2O_3(0001) consists of two aluminum layers separated by one oxygen layer (Fig. 4). Models built of several such MSS guarantee that the net dipole moment across the surface vanishes, resulting in a fast decay of the electrostatic potential outside the slab. This renders the interactions between the slabs in the periodic three-dimensional supercell model negligible [11, 57]. The two (outer) surfaces of a nine-layer (9L) slab of three MSS (Fig. 4) used

FIGURE 4. Schematic represenation of a nine-layer (9L) slab model of the α-Al$_2$O$_3$(0001) surface.

employed to construct supercells of a 3×3 hexagonal overlayer for studying adsorption complexes of H$_2$O [18].

After optimization of the slab structure the rigid ion approximation is abandoned for the ions in the active site of the regular surface a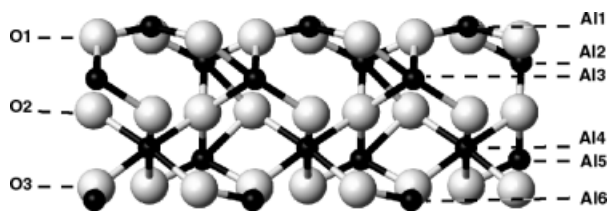nd in its vicinity (Regions I and IIa) to account for the polarization within the shell model [46]. Region IIa is defined as the collection of lattice centers with a maximum distance R $= 6$ Å from the outer atoms of Region I; it contains about 200 centers. An increase of the distance R to 9 or 12 Å results in insignificant changes of the observables calculated in Step 3: the adsorption energy of CO varies by less than 0.005 eV and the adsorption-induced frequency shift $\Delta\nu$(CO) changes by less than 0.3 cm^{-1}. For the system under study, consisting of regular (uncharged) sites on α-Al$_2$O$_3$(0001) and neutral adsorbate CO, Region IIb can be omitted if Region IIa is taken sufficiently large as is the case here. Therefore, only Regions IIa and IIc of the environment (Fig. 1) have been used in the present investigation.

In Step 2, *embedded* cluster calculations of the *unperturbed* surface site are carried out, relaxing the QM cluster model of the regular site to the equilibrium, but keeping the environment fixed at the reference structure determined in Step 1. The environment and the QM cluster are coupled both by the electrostatic (Madelung) field of *all* surrounding ions and the short-range pair potentials acting across the cluster boundary. Formal ionic charges, $+3e$ and $-2e$ for Al and O centers, respectively, are used to calculate the Madelung field. A three-dimensional Ewald summation is performed for repeated slabs separated by vacuum layers [59]. To calculate the matrix elements of the external electrostatic potential, we used a finite array of point charges located in symmetric fashion around the QM cluster. This array consists of a neutral set of PCs at lattice positions, PC, and a set of specially optimized PCs, located on a sphere S encompassing the QM cluster [60]. The array PC is constructed

from an extended unit cell of the substrate slab, symmetrized as for the construction of a Wigner–Seitz unit cell. The surface S is formally endowed with a surface density $\sigma(\mathbf{r})$ that satisfies the condition

$$V(\mathbf{r})\bigg|_S = \oint \frac{\sigma(\mathbf{r}')\,dS}{|\mathbf{r} - \mathbf{r}'|}, \qquad (12)$$

where $V(\mathbf{r})$ is the *electrostatic potential* of all PCs of the slab that make up the Madelung potential on the sphere S *minus* the contributions of the finite array PC; $V(\mathbf{r})$ is evaluated with the help of the Ewald method. No PCs located inside the sphere S contribute to the potential $V(\mathbf{r})$. If the condition of Eq. (12) is fulfilled, both the true Madelung potential and the potential arising from $\sigma(\mathbf{r}) + PC$ are *equal* everywhere inside S. After discretization of $\sigma(\mathbf{r})$ via a finite set of representative PCs q_j at grid positions $\mathbf{r}_j$, regularly distributed over S and associated with surface areas S_j, the integral equation Eq. (12) is reduced to a set of linear equations [61]:

$$V(\mathbf{r}_i) = \sum_j A_{ij} q_j$$

$$\text{with } A_{ij} = \begin{cases} 1.07(4\pi/S_j)^{1/2} & i = j \\ |\mathbf{r}_i - \mathbf{r}_j| & i \neq j. \end{cases} \qquad (13)$$

We explored grids derived from an octahedron inscribed in S with subsequent refinement of the surface triangles [62] as well as Lebedev's integration grids [63]. The external electrostatic field of the regular slab was represented by about 700 PCs including the set PC and PCs representing the charge distribution on surface S. In Table II we compare the external potential calculated at nuclei of symmetry-inequivalent atoms of the cluster $[\text{Al}_{10}\text{O}_{15}]/\text{Al}_{13}^{\text{PP}*}$ when the surface charge density is represented by 110 [63] or 128 [62] PCs q_j with the directly (exactly) calculated Madelung potential. The scheme with 128 surface point charges is slightly more accurate, but both models are sufficient for describing the Madelung field in the central part of the cluster (in a radius of $\sim$4.2 Å). A larger number of point charges would reduce the computational efficiency of the scheme to model the external field and thus is not warranted. The field of the regular slab is explicitly corrected for displacements resulting form the shell-model calculations (Step 3) due to the formation of a "defect."

The DF calculations have been carried out using the linear combination of Gaussian-type orbitals fitting-functions density functional (LCGTO-FF-DF) cluster method [64] implemented in the parallel computer code PARAGAUSS [43, 44]. Gradient-

TABLE II

Madelung potential V of a nine-layer slab at the atomic positions of the cluster $[Al_{10}O_{15}]/Al_{13}^{pp*}$ and deviations $\Delta V^{(n)}$ of the electrostatic potentials calculated for finite arrays of point charges including $n = 128$ or $n = 110$ points of the surface charge representation. Energies in a.u.

Atom[a]	R_b[b] (Å)	V	$\Delta V^{(128)} \times 10^4$	$\Delta V^{(n)} \times 10^4$
Al1	0.00	−1.3032	0	−1
O1	1.62	1.0491	0	−1
O2	2.80	0.9701	0	−1
Al2	2.91	−1.3764	−1	−1
Al3	3.05	−1.3541	0	−1
O1	3.17	1.0491	0	−1
Al4	3.20	−1.3541	−1	−2
O1	4.18	1.0491	0	−4
O1	4.22	1.0491	−2	−1
Al5	4.49	−1.3764	−7	−2
Al1	4.75	−1.3032	−14	−55
Al2	5.58	−1.3764	−44	−46
Al3	5.65	−1.3541	−60	−56

[a] Atomic labels indicate to which layer of the α-Al$_2$O$_3$ slab a given atom belongs.

[b] R—distance from the central Al1 atom of the cluster to a given atom [see Fig. 2(e)].

corrected functionals (generalized gradient approximation, GGA) have been used in a self-consistent fashion for the exchange [65] and the correlation energy [66]. The PARAGAUSS implementation of the EPE embedding scheme for treating the effect of a cluster environment has recently been discussed in detail elsewhere [9]. In the following, we will correct adsorbate-substrate binding energies for the basis set superposition error by applying the standard counterpoise method [67] in a single-point fashion at the equilibrium geometry of the adsorption complexes. The C, O, and Al basis sets were taken from a previous calculation of molecular models of Al$_2$O$_3$ [8]: C (9s5p2d) → [5s4p2d], O (CO) (9s5p2d) → [5s4p2d], and Al (12s9p2d) → [6s4p2d]. For the O centers of the substrate, a more flexible orbital basis was used (13s8p1d → 6s5p1d) [68]. All contractions were of the generalized, atomic form. The auxiliary basis sets used in the LCGTO-FF-DF method to represent the electron charge distribution when calculating the Hartree contribution to the electron–electron interaction were constructed in a standard fashion (5 p-type and 5 d-type exponents on all centers [64]). In our study of CO adsorption at the cation-terminated α-Al$_2$O$_3$(0001) surface, we fo-

cused on adsorbate configurations with the molecular axis oriented perpendicular to the surface and the carbon center pointing to the LAS. Force constants were computed as finite differences of directly calculated energy gradients; in the corresponding harmonic frequency analysis only two vibrational modes, C–O and substrate-CO, were explicitly taken into account.

Results and Discussion

STRUCTURAL FEATURES OF BULK AND SLAB MODELS OF α-ALUMINA

The crystal structure of α-alumina exhibits rhombohedral symmetry with a hexagonal unit cell (space group R3c). The lattice parameters $a = b = 4.757$ Å, $c = 12.988$ Å define the primitive unit cell containing 12 Al and 18 O atoms [69]. Ions are grouped along the c axis in an alternating stacking of two Al^{3+} layers and one O^{2-} layer (Fig. 4). The bulk cations Al^{3+} are situated in the octahedral sites of the hexagonal close-packed oxygen sublattice, slightly closer to one of the two oxygen layers. This arrangement yields three Al1–O1 distances at 1.86 Å and three Al2–O1 distances at 1.97 Å (Fig. 3). The cations occupy two-thirds of the octahedral positions. The oxygen sublattice is planar but slightly laterally distorted compared to a regular closed-packed lattice. There are large and small equilateral oxygen triangles with edges of 2.87 and 2.52 Å, respectively; the triangles in close contact with a cation are larger. Each oxygen atom of one layer has three neighbors from the next oxygen layer, at three different distances.

The relaxation of the α-Al$_2$O$_3$(0001) surface is crucial for understanding its properties. Both experimental [34, 38] and theoretical approaches show a strong distance reduction between the first (upper) and the second surface layers with respect to the interplane spacing in the bulk. However, the extent of the relaxation is rather differently quantified in various studies, ranging from 50 to 90% of the bulk interplane spacing [13]. Relaxation of the deeper surface layers is also described nonuniformly.

In a detailed structure of the α-Al$_2$O$_3$(0001) surface [34] a close-packed oxygen plane covered with a plane of Al^{3+} ions has been found, resulting in the 3:1 ratio of the numbers of O^{2-} to Al^{3+} ions in these upper two planes. Two major changes of the truncated-bulk surface are observed in the relaxed structure (Fig. 4) [34]: the distance between

TABLE III

Comparison of the bulk structure[a] of α-Al_2O_3 obtained from atomistic simulations with the structure derived from neutron diffraction[b] (exp).

A	B	z^{exp}	z	N_c	Δz^{exp}	Δz	$\Delta z^{exp} - \Delta z$	R^{exp}	R	$R^{exp} - R$
O1		0.84	0.76							
	O1(Al1)			2	0.00	0.00	0.00	2.87	2.90	−0.03
	O1(Al2)			2	0.00	0.00	0.00	2.87	2.90	−0.03
	O1(Al3)			2	0.00	0.00	0.00	2.52	2.47	0.05
	O2(Al3)			3	2.17	2.17	0.00	2.62	2.61	0.00
	O2(Al4)				2.17	2.17	0.00	2.73	2.74	0.00
	O2(Al5)				2.17	2.17	0.00	2.73	2.74	0.00
Al2		1.68	1.52							
	O1			3	0.84	0.76	0.08	1.86	1.84	0.02
	O2			3	1.33	1.41	−0.08	1.97	2.00	−0.03
	Al3			3	0.49	0.64	−0.15			

[a] z—interplane distances from a given layer of atoms A to the top Al1 layer; Δz—interplane distances from the layer of atoms B to the preceding layer of atoms A; R—distances from atom A to atoms B in the first coordination sphere of atom A; N_c—number of atoms of type B in coordination sphere of atom A. The labels in parentheses specify the cation, in the first coordination sphere of which the given anion is situated. All distances in Å.
[b] Reference [20].

the first, O1, and the second, O2, oxygen layers is increased and oxygen triangles change their size in a nonuniform fashion, so that three types of such triangles are formed. Those triangles in contact with cations of the top layer, Al1, become the largest, $R_s^{Al1}(O1–O1) = 2.99$ Å. The size of the O1 triangles contacting Al^{3+} cations of the second layer, Al2, decreases the most, $R_s^{Al2}(O1–O1) = 2.51$ Å, with respect to the bulk value of 2.87 Å; these triangles become the smallest. The edges of the third type of triangles (the smallest ones in the bulk, $R_b(O1–O1) = 2.52$ Å) increases to 2.77 Å. Notwithstanding the large change of the interlayer distance between the first and the second plane ($\Delta z_b − \Delta z_s = 0.43$ Å), the distance Al1–O1 decreases by 0.1 Å only. The strong shortening of the Al1–O1 interplane spacing from the refinement of the GIXS data, by 51% [34], is supported by results of HF (68% [42]; 59% [13]) and DF calculations (plane-wave representation of the valence orbitals: 86% [14], 84% [13], 77% [17]; Gaussian orbital approach: 87% [15]).

In Table III the structure of bulk α-alumina calculated with pair-potential parameters [56] is compared with experiment [20]. The AS model yields a satisfactory description of the structure. The oxygen triangles contacting the ions Al1 and Al2 are only slightly, by 0.03 Å, extended compared to experiment. The triangles contacting the cations Al3 of the next MSS are contracted by 0.05 Å. The nearest-

neighbor short and long Al–O distances, Al2–O1 and Al2–O2, differ from the experimental values by −0.02 and 0.03 Å, respectively. Thus, the force field [56] is able to reproduce the structure of bulk α-alumina fairly well.

Structural data for the 9L (Fig. 4) and 18L slabs are collected in Tables IV and V. The nearest-neighbor Al–O distances calculated for 9L slab, R_s^{9L}, at the AS level and those measured by GIXS for the surface [34], R_s^{exp}, compare to the corresponding bulk values R_b and R_b^{exp} as follows (see Table III for the experimental bulk values): Al1–O1 89% vs. 94%, Al2–O1 95% vs. 94%, Al2–O2 98% vs. 99%, Al3–O1 94% vs. 105%, Al3–O2 103% vs. 105%, Al4–O2 99% vs. 99%, respectively. Therefore, in relative terms, the atomic simulations reproduce pertinent structural changes satisfactorily. This reasonable agreement between the results of the classical AS approximation and experiment is due to the fact that the main driving force for relaxation and reconstruction of the strongly ionic system α-$Al_2O_3(0001)$ is classical electrostatics. The interlayer relaxation is accompanied by in-plane relaxations of the $O^{2−}$ ions; for an informative illustration of the in-plane relaxation see Ref. [17].

Some discrepancies between the AS description of the relaxation of the top MSS as compared to GIXS data are worth noting [34]. When going from the bulk to the surface, the interlayer distance $\Delta z(O1–O2)$ decreases by 0.19 Å at the AS level but

TABLE IV

Relaxation-induced alteration of interlayer distances[a] of the α-Al$_2$O$_3$(0001) surface calculated with 9L and 18L slabs and comparison with results from GIXS measurements.[b]

A	B	z_b	z_s^{9L}	z_s^{18L}	N_c	Δz_b	Δz_s^{9L}	Δz_s^{18L}	$\Delta z_b - \Delta z_s^{9L}$	$\Delta z_b - \Delta z_s^{18L}$	$\Delta z_b^{exp} - \Delta z_s^{exp}$
Al1		0.00	0.00	0.00							
	O1				3	0.76	0.29	0.34	0.47	0.42	0.43
O1		0.76	0.29	0.34							
	O1(1)				2	0.00	0.00	0.00	0.00	0.00	0.00
	O1(2)				2	0.00	0.00	0.00	0.00	0.00	0.00
	O1(3)				2	0.00	0.00	0.00	0.00	0.00	0.00
	O2				3	2.17	1.98	1.96	0.19	0.21	−0.17
Al2		1.52	0.98	1.05							
	O1				3	0.76	0.69	0.71	0.07	0.05	−0.14
	O2				3	1.41	1.29	1.25	0.12	0.16	−0.03
Al3		2.17	1.33	1.41							
	O1				3	1.41	1.04	1.08	0.37	0.33	0.00
	O2				3	0.76	0.94	0.89	−0.18	−0.13	−0.17

[a] Subscripts b and s denote data for bulk and surface models, respectively. For further explanations of the data structure and the notation see Table III. All distances in Å.
[b] Reference [34].

increases by 0.17 Å in the experiment (Table IV). Also, the computed contraction of the oxygen triangles at Al2 is less significant than in experiment. Moreover, on the surface the oxygen triangles at Al1 are shrunk at the AS level, by 4.4%, at variance with their measured extension by 4.2%. The force-field result agrees with a DF result on a periodic model (3.2%) [17]. While the measured increase of the in-

TABLE V

Interatomic distances[a] of the α-Al$_2$O$_3$(0001) surface and their relaxation-induced alteration calculated with 9L and 18L slab models and comparison to results of GIXS measurements.[b]

A	B	N_c	R_b	R_s^{9L}	R_s^{18L}	$R_b - R_s^{9L}$	$R_b - R_s^{18L}$	$R_b^{exp} - R_s^{exp}$
Al1								
	O1	3	1.84	1.63	1.63	0.21	0.21	0.09
O1								
	O1(1)	2	2.90	2.77	2.75	0.13	0.15	−0.12
	O1(2)	2	2.90	2.76	2.78	0.14	0.12	0.36
	O1(3)	2	2.47	2.71	2.71	−0.24	−0.24	−0.25
	O2(3)	3	2.61	2.49	2.48	0.12	0.13	−0.08
	O2(4)		2.74	2.51	2.50	0.23	0.24	−0.03
	O2(5)		2.74	2.61	2.61	0.13	0.13	−0.27
Al2								
	O1	3	1.84	1.74	1.76	0.10	0.08	0.12
	O2	3	2.00	1.95	1.91	0.05	0.09	0.01
Al3								
	O1	3	2.00	1.88	1.90	0.12	0.10	−0.11
	O2	3	1.84	1.90	1.91	−0.06	−0.07	−0.10

[a] Subscripts b and s denote data for bulk and surface, respectively. For further explanations of the data structure and the notation see Table III. All distances in Å.
[b] Reference [34].

terlayer distance Δz(O1–Al2), by 18% when going from the bulk to the surface, is in line with the DF result (increase by 16%) [17], the force-field calculations yield a slight decrease, by −7%. However, for ions of these two layers, alterations of the nearest-neighbor distances R(O1–Al2) are well reproduced by the AS: 0.12 Å GIXS vs. 0.08 Å AS. As discussed elsewhere [17], the interlayer spacing Δz(O1–Al2) is not reproduced in most calculations reported to date; it seems to be an energetically subtle effect.

More importantly, the measured changes of the nearest-neighbor distances between bulk and surface, R_b^{exp}(Al2–O1) − R_s^{exp}(Al2–O1) = 0.12 Å and R_b^{exp}(Al1–O1) − R_s^{exp}(Al1–O1) = 0.09 Å, are qualitatively correctly reproduced in the AS approximation, 0.10 and 0.21 Å, respectively. Also, the change of the distances between the first two layers of the surface, 0.43 Å [34], is close to that of AS, 0.47 Å. Similar values were calculated recently by the HF method for 6L and 12L slabs, 0.42 and 0.47 Å, respectively [13]. In the following, only results for cluster embedded in the 9L slab will be discussed.

DESIGN OF CLUSTER MODELS OF LAS AT α-Al$_2$O$_3$(0001)

The surface α-Al$_2$O$_3$(0001) consists of a network of four types of oxygen triangles, different in size. Half of the triangle sites are filled with Al^{3+} cations. The oxygen anions of the sites not occupied by cations form, together with the nearby anions of the underlying MSS, empty tetrahedral cavities. The other three types of the triangles are occupied by Al^{3+} cations of the layers Al1, Al2, and Al3 (Fig. 5). Only the first type of sites with Al^{3+} cations above the upper oxygen layer is of interest as surface LAS. The cluster models of LAS studied here, [Al$_7$O$_3$]$^{15+}$ [Fig. 2(a)], [Al$_4$O$_6$]/Al$_6^{pp*}$ [Fig. 2(b)–(d)],
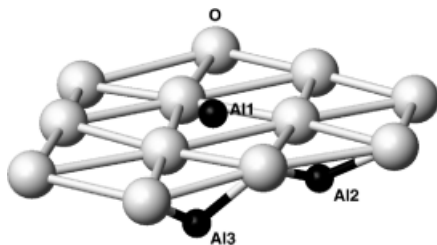

FIGURE 5. Fragment of the Al-terminated α-Al$_2$O$_3$(0001) surface displaying four different oxygen triangle sites. All O ions are in the (0001) plane, the center Al1 is above that plane, Al2 is below, and Al3 is lower than the plane Al2.

[Al$_{10}$O$_{15}$]/Al$_{13}^{pp*}$ [Fig. 2(e), (f)], are all centered on Al1 cations. The first two clusters are subsystems of the largest cluster [Al$_{10}$O$_{15}$]/Al$_{13}^{pp*}$. The cluster [Al$_7$O$_3$]$^{15+}$ **a** includes all three anions of the first coordination sphere of the central Al^{3+} and six cations of the second coordination sphere so that all anions are completely coordinated by nearest neighbors. Cluster **a** is not stoichiometric. The stoichiometric clusters [Al$_4$O$_6$]/Al$_6^{pp*}$ **b**–**d** contain three more oxygen anions of the top layer. The coordination spheres of the oxygen anions are completed by regular Al atoms and by bare pseudopotentials Al^{pp*}. In cluster **b**, bare pseudopotentials are used to represent the cations of the layers Al2 and Al3. All cations of the top layer Al1 are represented by regular all-electron atoms with basis functions. The electronic state of the top layer cations of the relaxed surface is not expected to differ significantly from that of cations in the bulk, based on band structure calculations [14, 17, 42]. Therefore, cluster model **b** is assumed to be suited better for describing possible changes in the electronic state of the surface cations than the other two models **c** and **d** of the same stoichiometry [Al$_4$O$_6$]/Al$_6^{pp*}$. The nearest-neighbor anions of the central Al atom are most favorably coordinated in cluster **c**: all cations of the top MSS contacting these anions are atoms with basis functions. The cations Al3 occupying the third place of the first coordination sphere of the anions—from the neighboring MSS—are located at a longer distance than Al1 and Al2 centers. Cluster **d** represents the third and the last possible variant of the model [Al$_4$O$_6$]/Al$_6^{pp*}$. The three anions closer to the Al center of this cluster are coordinated by bare pseudopotentials Al2^{pp*} at closer distances and by cations Al3 with basis functions a longer distances; thus, we consider this cluster inferior to the clusters **b** and **c**. The extended clusters [Al$_{10}$O$_{15}$]/Al$_{13}^{pp*}$ **e** and **f** are stoichiometric and include all atoms of the clusters [Al$_4$O$_6$]/Al$_6^{pp*}$ as a fragment. In cluster **f** all cations of the smaller clusters [Al$_4$O$_6$]/Al$_6^{pp*}$ are described at the all-electron level, so that the anions of the first and second coordination spheres are in contact with regular (all-electron) atoms only. In cluster **e**, three Al3 cations of the second MSS are exchanged (compared to cluster **f**) by terminal bare pseudopotentials so that all top layer cations are regular.

The gap between the highest occupied and the lowest unoccupied molecular orbitals (HOMO–LUMO) of all clusters modeling a LAS is reasonably large, 5–6 eV, as is typical for the surface of a wide gap insulator. The gap reflects the absence of artificial frontier states that might be formed

due to boundary conditions imposed on the QM cluster. The forbidden gap in local density band structure calculations is 6.22 eV at the Γ point for bulk α-Al_2O_3 [15]. Gaps of insulators are usually underestimated by about 30% with common exchange-correlation functionals [70]. The gap at the surface of α-Al_2O_3 has recently been measured to be $\sim$6 eV [71] and 7–8 eV [72]. When going from $[Al_4O_6]/Al_6^{PP*}$ clusters to larger clusters $[Al_{10}O_{15}]/Al_{13}^{PP*}$ the HOMO–LUMO gap changes by at most 0.2 eV. Substitution of a part of the cations by bare pseudopotentials in the cluster $[Al_{10}O_6]^{18+}$ to ensure its stoichiometry results in a uniform upward shift of all one-electron eigenvalues by about 1 eV. This is a consequence of the fact that the electron density cannot be withdrawn from the oxygen anions by centers without basis functions such as Al^{PP*}.

In Step 2 of the embedding procedure, the geometry of the clusters modelling the regular α-$Al_2O_3(0001)$ surface is optimized. The equilibrium QM cluster geometry (Table VI) is somewhat different from the geometry of the AS description. This is not unexpected because the equilibrium structure of the crystal at the DF level differs from that obtained in the AS approach [13].

From now on, we discuss the observables of the cluster $[Al_{10}O_{15}]/Al_{13}^{PP*}$ **f**, unless explicitly mentioned otherwise. The distances Al1–O1 are larger in the embedded cluster calculations, about 1.70 Å, compared to the AS value of 1.63 Å, but they are still shorter than the GIXS value of 1.77 Å [34]. The distances O1–Al2, $\sim$1.78 Å, are only slightly longer than the AS and GIXS values 1.74 Å. The

distances O1–Al3 are calculated at 1.87 and 1.90 Å in the central and terminal regions of the cluster, respectively—rather close to the AS value 1.88 Å. The much longer GIXS value 2.08 Å is likely overestimated.

The contraction of the interplane distance Δz(O1–Al1) is usually taken as a measure of relaxation for the cation-terminated α-$Al_2O_3(0001)$ surface [13]. This distance Δz(O1–Al1), calculated to be about 0.20 Å, is smaller than the values obtained at the AS level, 0.29 Å, and with GIXS, 0.41 Å [34]. Inspection of Table VI shows that Δz increases from 0.18–0.19 to 0.22–0.23 Å with increase of the cluster size. In a GGA DF calculation on a periodic model of an 18L slab a Δz value of 0.14 Å was obtained [13]. This value is in line with our EPE embedded cluster distances. Thus, there is evidence that the GIXS value is overestimated. Time-of-flight scattering and recoiling spectrometry as well as classical ion trajectory simulations yield a Δz value of 0.3 $\pm$ 0.1 Å [38]. The other interplane distances calculated with the EPE approach, Δz(Al2–O1) = 0.73 Å and Δz(Al3–O1) = 1.13 Å, are in closer agreement with the corresponding AS distances of 0. 69 and 1.04 Å while the values obtained in DF band structure calculations are 0.83 and 1.10 Å, respectively [13]. Thus, the various computational approaches exhibit acceptable agreement for the relaxed structure of the surface α-$Al_2O_3(0001)$, among each other and with available experimental data [13, 38].

ADSORPTION COMPLEXES WITH CO

One commonly assumes that one can identify isolated low-coordinated cations on metal oxide surfaces via blue shifts of the vibrational frequency of CO probe molecules adsorbed on them [4]. Recently, there have been several computational studies of such adsorption complexes, in particular on MgO surfaces [73–75]. However, on polar surfaces of transition metal oxides, like α-Cr_2O_3, similar bands with $\Delta\nu$(CO) $\sim$ 40 cm^{-1} were assigned to various adsorption complexes at regular (not low-coordinated) surface sites including those exhibiting (strongly) inclined CO molecules [76–80]. Several factors affect the CO adsorption on polar surfaces like α-$Al_2O_3(0001)$. The dipole moment associated with the creation of a simple bulk-terminated surface with cations in the top layer produces a steplike decay of the electrostatic potential on going from the crystal to vacuum. This spatial characteristic of the electrostatic potential tends to increase the CO bond length as well as to reduce the frequency ν(CO) [9].

TABLE VI

Calculated interplane O1-Al1 (Δz) and interatomic distances $r(A–B)$ from atomistic simulations (AS) and EPE cluster models (Fig. 2) of surface Lewis acid sites. Distances in Å.

| | | Embedded clusters | | | | |
| | | $[Al_4O_6]/Al_6^{PP*}$ | | | $[Al_{10}O_{15}]/Al_{13}^{PP*}$ | |
Distance	AS	b	c	d	e	f
r_1(O1–Al1)	1.63	1.70	1.71	1.71	1.70	1.70
r_2(O1–Al3)	1.88	1.85	1.89	1.83	1.89	1.87
r_3(O1–Al2)	1.74	1.75	1.74	1.77	1.77	1.78
r_4(O1–Al2)	1.74	1.76	1.74	1.77	1.77	1.77
r_5(O1–Al3)	1.88	1.86	1.86	1.83	1.92	1.90
r_6(O1–Al1)	1.63	1.67	1.69	1.69	1.68	1.68
Δz	0.29	0.19	0.18	0.18	0.23	0.22

On the other hand, if the top layer Al^{3+} cations were partially reduced by electron transfer from O^{2-} anions of the layer underneath and the surface relaxes with a contraction of the Al1-O1 interlayer distance, then the C–O distance would shorten with a concomitant blue shift of the CO vibrational frequency. The interplay of these factors defines the actual structural, binding, and vibrational parameters of adsorbed CO. Thus, computational investigations based on EPE embedded cluster models help to assert and interpret the adsorption properties of LAS on the α-Al_2O_3(0001).

From the computational point of view, the way the interactions between the boundary anions of the cluster and the cations of the environment are described is an important factor influencing the properties of CO adsorption complexes. The interaction of CO with LAS of the surface α-Al_2O_3(0001) is local. Therefore, size limitations of the QM cluster should not be crucial as soon as the perturbation of the adsorption site due to the cluster borders becomes small. Note that the use of regular Al atoms with basis functions to represent Al^{3+} centers in the frontier region of (usually nonstoichiometric) clusters may result in a biased description of adsorption properties when the bonding within the substrate features covalent contributions. The central region of the QM cluster in such a case would acquire an artificial electron-deficient character due to electron transfer to the frontier cations included in the cluster in excess of its stoichiometry. In calculations of the model $[Al_7O_3]^{15+}$ with such embedding using only regular Al centers on the cluster border, the blue shift of CO frequency is as big as 42 cm^{-1} (Table VII). Therefore, this frequency shift and a binding energy of 0.49 eV are probably the upper limits for the calculated results of these observables among the series of clusters under consideration, differing by the representation of their cluster boundaries.

The shift $\Delta\nu$(CO) decreases when bare pseudopotentials saturate the first coordination sphere of the anions and thus restore the stoichiometricity of the cluster model. For CO on the clusters $[Al_4O_6]/Al_6^{pp*}$ (**b–d**) the frequency shift is about 10 cm^{-1} smaller than that of the adsorption complex with $[Al_7O_3]^{15+}$ (Table VII). A shift $\Delta\nu$(CO) of 29 cm^{-1} is calculated for the cluster $[Al_4O_6]/Al_6^{pp*}$ **b** with basis functions on all cations of the top layer. For cluster **c** with basis functions on the cations of the first MSS that coordinate three oxygen anions in the center of cluster, one obtains $\Delta\nu$(CO) = 28 cm^{-1}. The CO vibrational shift of the cluster **d** with three regular Al cations moved into

TABLE VII

Calculated characteristics[a] of CO adsorption complexes on Al^{3+} centers of the α-Al_2O_3(0001) surface.

Model[b]		$\Delta\nu$(CO)[c]	BE	r_e(C–O)	r_e(C–Al)
$[Al_7O_3]^{15+}$	**a**	42	0.49	1.134	2.184
$[Al_4O_6]/Al_6^{pp*}$	**b**	29	0.38	1.134	2.206
$[Al_4O_6]/Al_6^{pp*}$	**c**	28	0.37	1.135	2.202
$[Al_4O_6]/Al_6^{pp*}$	**d**	30	0.38	1.135	2.198
$[Al_{10}O_{15}]/Al_{13}^{pp*}$	**e**	42	0.43	1.134	2.191
$[Al_{10}O_{15}]/Al_{13}^{pp*}$	**f**	38	0.41	1.134	2.206

[a] Adsorption-induced CO frequency shift $\Delta\nu$(CO) (in cm^{-1}), binding energy BE (in eV), and bond lengths r_e (Å).
[b] For sketches of the cluster models see Figure 2.
[c] The calculated reference harmonic frequency of free CO is 2122 cm^{-1}. Reported measured shifts are 39 cm^{-1} [4] and ~20 cm^{-1} [7].

the third layer of the model is calculated at 30 cm^{-1}. Hence, the calculated CO frequencies of all adsorption complexes involving all clusters of the type $[Al_4O_6]/Al_6^{pp*}$ fall in a narrow range of 3 cm^{-1}. The calculated frequency shifts increase when one goes to the extended clusters $[Al_{10}O_{15}]/Al_{13}^{pp*}$ **e** and **f**. For adsorption on the cluster **f** with a central region where all cations bear basis functions, the frequency shift is 38 cm^{-1}. Model $[Al_{10}O_{15}]/Al_{13}^{pp*}$ **e**, which is probably best suited to reproduce a conceivable charge transfer in the top two layers because all Al cations of the top layer of the cluster bear basis functions, yields a frequency shift of 42 cm^{-1}. Similar to the vibration frequency shifts, the adsorption energies calculated with the cluster models **b–f** also fall in a narrow interval of ~0.05 eV (1 kJ/mol) close to the value 0.4 eV (Table VII). The fact that calculated characteristics of the CO adsorption complexes are quite stable in this series of differing cluster models lends credibility to the quality of the EPE embedding procedure.

A moderate experimental blue frequency shift of CO interacting with LAS of α-alumina ~20 cm^{-1} has been reported [7]. The IR band measured at 77 K and a CO pressure of 40 Torr was assigned to CO interacting with surface Al^{3+} ions via a weak σ bond. No appreciable shift of the frequency was observed for decreasing CO coverage. At variance with this finding, another experimental group observed a notable coverage dependence of the C–O frequency, connected to CO adsorption at extended

terraces; these alternative measurements on CO adsorbed on powder α-Al_2O_3 crystallites yielded a shift $\Delta\nu(CO) = 39\,cm^{-1}$ in the low pressure limit [4]. The CO frequency shift is a very sensitive indicator of delicate adsorbate-substrate interactions. Hence, it is satisfying to note that calculations on the most realistic cluster models $[Al_{10}O_{15}]/Al_{13}^{PP*}$ considered here yield frequency shifts of 38–42 cm^{-1}, in very good agreement with the latter experimental result. From this comparison it follows that the adsorption properties of the α-$Al_2O_3(0001)$ surface are well reproduced by the present models which employ a consistent embedding scheme in an EPE.

It is interesting to note that the adsorption properties of the three-coordinated Al^{3+} centers of α-$Al_2O_3(0001)$ with strong lateral Coulomb interactions are similar to those of isolated three-coordinated Mg^{2+} cations at corner positions of MgO crystallites where such lateral interactions are absent. For the latter system a CO binding energy of 0.38 eV and a CO vibrational frequency shift of 39 cm^{-1} were calculated with the GGA DF method employed here, yet with less sophisticated cluster embedding [51]. The corner Mg^{2+} cations relax inward only moderately because the structure of MgO corners is rather rigid. On the other hand, the inward ("downward") displacement of Al^{3+} cations on the flexible α-$Al_2O_3(0001)$ surface is large. This strong relaxation ultimately dominates and results in a blue shift of the CO frequency while the charge separation (a major feature of polar cation-terminated surface) actually acts in the opposite direction, shifting the CO frequency to longer wave lengths [37].

Conclusions

We have applied a density functional approach that utilizes a recently implemented consistent embedding of QM clusters in a crystal environment described by means of classical AS modelling to study adsorption complexes of CO on the strongly relaxed polar cation-terminated α-$Al_2O_3(0001)$ surface. The Madelung field is calculated accurately via an expansion of the external potential with the help of an optimized (discretized) surface charge distribution on a sphere that surrounds the QM cluster. The AS method provides the structure of surface that is accurate enough to embed the DF clusters and to produce results that are reasonably well converged with respect to the cluster

size. Therefore, we conclude that perturbations of the electronic structure in the central region of the clusters due to the cluster boundaries are rather weak. Discrepancies between the DF and AS descriptions of the relaxation effect do not appreciably affect the calculated adsorption parameters. The calculated adsorption-induced shifts of the CO vibration frequency on models of LAS represented by three coordinated surface cations, 30–42 cm^{-1}, agree with the experimental values of the shift, 20–39 cm^{-1} [4, 7]. Note that the frequency shift calculated with EPE embedded clusters is notably, by 20–40 cm^{-1}, lower than that for molecular models [8]. The three-coordinated Al^{3+} centers of the surface α-$Al_2O_3(0001)$ exhibit similar adsorption properties as isolated low-coordinated Mg^{2+} cations in the corner positions of MgO [51], namely both for the adsorption energy, 0.40–0.49 eV vs. 0.38 eV, and the vibrational frequency shift, 30–40 cm^{-1} vs. 39 cm^{-1}, of CO at α-$Al_2O_3(0001)$ and MgO, respectively.

The present study shows a good performance of the variational EPE embedding method: it adequately models the adsorption properties of polar surfaces of ionic metal oxides, where considerable relaxation cannot be efficiently described in less sophisticated embedding approaches. We have also recently demonstrated the advantages of this consistent EPE embedding for studying interactions of (charged) surface defect sites on MgO with metal atoms [9]. Based on the results of these two investigations we conclude that cluster models designed at this high level of accuracy open an excellent opportunity to successfully describe various types of surfaces and surface sites of ionic oxides as well as of adsorption interactions with them. This is particularly important for disordered surfaces and charged defect sites which are quite common in real oxide systems. For such adsorption problems, slab models with periodic boundary conditions can hardly offer an acceptable alternative to such realistic cluster models.

References

1. Dörre, E. Alumina; Springer: Berlin, 1984.

2. French, R. H.; Heuer, A. H. J Am Ceram Soc 1994, 77, 292.

3. Gates, B. C. Chem Rev 1995, 95, 511–522.

4. Paukshtis, E. A. Infrared Spectroscopy in Heterogeneous Acid-Base Catalysis (in Russian); Nauka: Novosibirsk, 1992.

5. Knözinger, H.; Ratnasamy, P. Catal Rev Sci Eng 1978, 17, 31–70.

6. Gatta, G. D.; Fubini, B.; Ghiotti, G.; Morterra, C. J Catal 1976, 43, 90–98.

7. Zecchina, A.; Platero, E. E.; Areán, C. O. J Catal 1987, 107, 244–247.

8. Neyman, K. M.; Nasluzov, V. A.; Zhidomirov, G. M. Catal Lett 1996, 40, 183–188.

9. Nasluzov, V. A.; Rivanenkov, V. V.; Gordienko, A. B.; Neyman, K. M.; Birkenheuer, U.; Rösch, N. J Chem Phys 2001, 115, 8157–8171.

10. Blonski, S.; Garofalini, S. H. Surf Sci 1993, 295, 263–274.

11. Catlow, C. R. A.; Gay, D. H.; Nygren, M. A.; Sayle, D. C. In Chemisorption and Reactivity on Supported Clusters and Thin Films, NATO ASI Series E, Vol. 331; Lambert, R; Pacchioni, G., Eds.; Kluwer: Dordrecht, 1997; pp. 479–521.

12. Streitz, F.; Mintmire, J. W. Phys Rev B 1994, 50, 11996–12003.

13. Baxter, R.; Reinhardt, P.; López, N.; Illas, F. Surf Sci 2000, 445, 448–460.

14. Manassidis, I.; de Vita, A.; Gillan, M. J. Surf Sci 1993, 285, L517–L521.

15. Verdozzi, C.; Jennison, D. R.; Schultz, P. A.; Sears, M. P. Phys Rev Lett 1999, 82, 799–802.

16. Wang, X. G.; Weiss, W.; Shaikhutdinov, S. K.; Ritter, M.; Petersen, M.; Wagner, F.; Schlögl, R.; Scheffler, M. Phys Rev Lett 1998, 81, 1038–1041.

17. Batyrev, I.; Alavi, A.; Finnis, M. W. Faraday Discuss 1999, 114, 33–43.

18. Hass, K. C.; Schneider, W. F.; Curioni, A.; Andreoni, W. J Phys Chem B 2000, 104, 5527–5540.

19. Wells, A. F. Structural Inorganic Chemistry; Oxford University: Oxford, 1984.

20. Wang, X. L.; Hubbard, C. R.; Alexander, K. B.; Becher, P. F. J Am Ceram Soc 1994, 6, 1569–1575.

21. Gomes, J. R. B.; Illas, F.; Hernández, N. C.; Márquez, A.; Sanz, J. F. Phys Rev B 2002, in press.

22. Mackrodt, W. C.; Davey, R. J.; Black, S. N.; Docherty, R. J Cryst Growth 1987, 80, 441–446.

23. Tasker, P. W. Adv Ceram 1988, 10, 176.

24. Mackrodt, W. C. J Chem Soc Faraday Trans 2 1989, 85, 541–554.

25. Catlow, C. R. A.; James, R.; Mackrodt, W. C.; Stewart, R. F. Phys Rev B 1982, 25, 1006–1026.

26. Salasco, L.; Dovesi, R.; Orlando, R.; Causà, M.; Saunders, V. R. Mol Phys 1991, 72, 267–277.

27. Sousa, C.; Illas, F.; Pacchioni, G. J Chem Phys 1993, 99, 6818–6823.

28. Pacchioni, G.; Sousa, C.; Illas, F.; Pamigiani, F.; Bagus, P. S. Phys Rev B 1993, 48, 11573–11582.

29. Guo, J.; Ellis, D. E.; Lam, D. J.; Phys Rev B 1992, 45, 3204–3214.

30. Miguel, M. A. S.; Sanz, J. F.; Alvarez, L. J.; Odriozola, J. A. Phys Rev B 1998, 58, 2369–2371.

31. Neyman, K. M.; Pacchioni, G.; Rösch, N. In Recent Developments and Applications of Modern Density Functional Theory; Seminario, J., Ed.; Elsevier: Amsterdam, 1996; Vol. 4; pp. 569–619.

32. Freund, H.-J. Faraday Discuss 1999, 114, 1–31.

33. Henry, C. R. Surf Sci Rep 1998, 31, 231–325.

34. Renaud, G. Surf Sci Rep 1998, 32, 1–90.

35. Rohr, R.; Bäumer, M.; Freund, H.-J.; Mejias, J. A.; Staemmler, V.; Müller, S.; Hammer, L.; Heinz, K. Surf Sci 1997, 372, 291–297. Erratum: ibid., 1997, 389, 391.

36. Goodman, D. W. J Vac Sci Technol A 1996, 14, 1526–1531.

37. Nasluzov, V. A.; Rivanenkov, V. V.; Shor, A.; Neyman, K. M.; Rösch, N. to be published.

38. Ahn, J.; Rabalais, J. W. Surf Sci 1997, 388, 121–131.

39. Walters, C. F.; McCarty, K. F.; Soares, E. A.; Van Hove, M. A. Surf Sci 2000, 464, L732–L738.

40. Sohlberg, K.; Pennycook, S.; Pantelides, S. J Am Chem Soc 1999, 121, 7493–7499.

41. Jaeger, R. M.; Kuhlenbeck, H.; Freund, H.-J.; Wuttig, M.; Hoffmann, W.; Franchy, R.; Ibach, H. Surf Sci 1991, 259, 235–252.

42. Puchin, V. E.; Gale, J. D.; Shluger, A. L.; Günster, E. K. J.; Brause, M.; Kempter, V. Surf Sci 1997, 370, 190–200.

43. Belling, T.; Grauschopf, T.; Krüger, S.; Mayer, M.; Nörtemann, F.; Staufer, M.; Zenger, C.; Rösch, N. In High Performance Scientific and Engineering Computing, Lecture Notes in Computational Science and Engineering; Bungartz, H.-J.; Durst, F.; Zenger, C., Eds.; Springer: Heidelberg, 1999; Vol. 8, pp. 439–453.

44. Belling, T.; Grauschopf, T.; Nörtemann, F.; Staufer, M.; Mayer, M.; Nasluzov, V. A.; Birkenheuer, U.; Hu, A.; Matveev, A.; Rösch, N. PARAGAUSS, version 2.1; Technische Universität München, 1999.

45. Lidiard, A. B. J Chem Soc Faraday Trans 2 1989, 85, 341–349.

46. Catlow, C. R. A.; Mackrodt, W. C. In Computer Simulation of Solids, Lecture Notes in Physics, Vol. 166; Catlow, C. R. A.; Mackrodt, W. C., Eds.; Springer: Berlin, 1982; pp. 3–20.

47. Wittbrodt, J. M.; Hase, W. L.; Schlegel, H. B. J Phys Chem B 1998, 102, 6539–6548.

48. Shapovalov, V.; Truong, T. N. J Phys Chem B 2000, 104, 9859–9863.

49. Felice, R. D.; Northrup, J. E. Phys Rev B 1999, 60, 16287–16290.

50. Hass, K. C.; Schneider, W. F.; Curioni, A.; Andreoni, W. Science 1998, 282, 265–268.

51. Yudanov, I. V.; Nasluzov, V. A.; Neyman, K. M.; Rösch, N. Int J Quantum Chem 1997, 65, 976–986.

52. Ferrari, A. M.; Pacchioni, G. Int J Quantum Chem 1996, 58, 241–250.

53. Xu, X.; Nakatsuji, H.; Ehara, M.; Lü, X.; Wang, N. Q.; Zhang, Q. E. Chem Phys Lett 1998, 292, 282–288.

54. Mejias, J. A.; Oviedo, J.; Sanz, J. F. Chem Phys 1995, 191, 133–139.

55. Hamann, D. R. Phys Rev B 1989, 40, 2980–2987.

56. Lewis, G. V.; Catlow, C. R. A. J Phys C 1985, 18, 1149–1161.

57. Fripiat, J. G.; Lucas, A. A.; Andre, J. M.; Derouane, E. G. Chem Phys 1977, 21, 101–104.

58. Gillan, M. J.; Manassidis, I.; de Vita, A. Philos Mag B 1994, 69, 879–888.

59. Deem, M. W.; Newsam, J. M.; Sinha, S. K. J Phys Chem 1990, 94, 8356–8359.

60. Stefanovich, E. V.; Truong, T. N. J Phys Chem B 1998, 102, 3018–3022.

61. Klamt, A.; Schüürmann, G. J. Chem Soc Perkin Trans 2 1993, 799–805.

62. Silla, E.; Tunon, I.; Pascual-Ahuir, J. L. J Comput Chem 1991, 12, 1077–1088.

63. Lebedev, V. I. J Comput Math Phys 1975, 15, 48; 1976, 16, 293.

64. Dunlap, B.; Rösch, N. Adv Quant Chem 1990, 21, 317–339.

65. Becke, A. Phys Rev A 1988, 38, 3098–3100.

66. Perdew, J. Phys Rev B 1986, 33, 8822–8824; 1986, 34, 7406.

67. Boys, S. F.; Bernardi, F. Mol Phys 1970, 19, 553–566.

68. Ferrari, A. M.; Xiao, C.; Neyman, K. M.; Pacchioni, G.; Rösch, N. Phys Chem Chem Phys 1999, 1, 4655–4662.

69. Kirfel, A.; Eichhorn, K. Acta Cryst A 1990, 46, 271–284.

70. Heaton, R. A.; Harrison, J. G.; Lin, C. C. Phys Rev B 1983, 28, 5992–6007.

71. Xu, C.; Lai, X.; Goodman, D. W. Faraday Discuss 1996, 105, 247–261.

72. Andersson, S.; Brühwiler, P. A.; Sandell, A.; Frank, M.; Libuda, J.; Giertz, A.; Brena, B.; Maxwell, A. J.; Bäumer, M.; Freund, H.-J.; Mårtensson, N. Surf Sci 1999, 442, 964–970.

73. Illas, F.; Pacchioni, G.; Pelmenschikov, A. G.; Pettersson, L. G. M.; Dovesi, R.; Pisani, C.; Neyman, K. M.; Rösch, N. Chem Phys Lett 1999, 306, 202–204.

74. Pelmenschikov, A. G.; Morosi, G.; Gamba, A.; Coluccia, S. J Phys Chem B 1998, 102, 2226–2231.

75. Soave, R.; Pacchioni, G. Chem Phys Lett 2000, 320, 345–351.

76. Scarano, D.; Zecchina, A. Spectr Acta A 1987, 43, 1441–1445.

77. Scarano, D.; Zecchina, A.; Reller, A. Surf Sci 1988, 198, 11–25.

78. Scarano, D.; Ricchiardi, G.; Bordiga, S.; Galletto, P.; Lamberti, C.; Spoto, G.; Zecchina, A. Faraday Discuss 1996, 105, 119–138.

79. Xu, C.; Dillmann, B.; Kuhlenbeck, H.; Freund, H.-J. Phys Rev Lett 1991, 67, 3551–3554.

80. Freund, H.-J. Angew Chem Int Ed Engl 1997, 36, 452–475.